Thermal lens evolution and compensation in a high power KGW Raman laser

Aaron McKay,* Ondrej Kitzler, and Richard P. Mildren

MQ Photonics Research Centre, Department of Physics and Astronomy Faculty of Science, Macquarie University Sydney New South Wales 2109 Australia
aaron.mckay@mq.edu.au

Abstract: The transient thermal lens in a high-average power double metal tungstate Raman laser has been investigated. An external cavity potassium gadolinium tungstate (KGW) laser designed for second-Stokes output was burst-pumped with up to 46 W of average power at a pulse repetition rate of 38 kHz. At low duty-cycle, the laser generated up to 18 W of on-time average Raman power with a conversion efficiency of 40%. At high duty cycle, efficiency is reduced and the near-field beam profile expands in the X_1' crystal direction over a period of tens of milliseconds. The evolution of the spatial beam properties occurs in response to the development of a highly astigmatic thermal lens with fast-axis susceptibility of approximately $-1.7\ m^{-1}$ per watt of Raman output power. We show that the likely cause for astigmatism is primarily photo-elastic in origin. Beam circularization was achieved by incorporating an intracavity convex cylindrical lens.

OCIS codes: (140.3550) Lasers, Raman; (140.6810) Thermal effects; (160.3380) Laser materials; (140.3538) Lasers, pulsed; (290.5910) Scattering, stimulated Raman; (190.4870) Photothermal effects.

References and links

1. S. Chénais, F. Druon, S. Forget, F. Balembois, and P. Georges, "On thermal effects in solid-state lasers: The case of ytterbium-doped materials," Prog. Quantum Electron. **30**(4), 89–153 (2006).
2. H. M. Pask, S. Myers, J. A. Piper, J. Richards, and T. McKay, "High average power, all-solid-state external resonator Raman laser," Opt. Lett. **28**(6), 435–437 (2003).
3. A. S. Grabtchikov, V. A. Lisinetskii, V. A. Orlovich, M. Schmitt, R. Maksimenka, and W. Kiefer, "Multimode pumped continuous-wave solid-state Raman laser," Opt. Lett. **29**(21), 2524–2526 (2004).
4. V. A. Lisinetskii, T. Riesbeck, H. Rhee, H. J. Eichler, and V. A. Orlovich, "High average power generation in barium nitrate Raman laser," Appl. Phys. B **99**(1–2), 127–134 (2010).
5. R. Chulkov, V. Lisinetskii, O. Lux, H. Rhee, S. Schrader, H. J. Eichler, and V. Orlovich, "Thermal aberrations and high power frequency conversion in a barium nitrate Raman laser," Appl. Phys. B **106**(4), 867–875 (2012).
6. T. T. Basiev, A. V. Gavrilov, V. V. Osiko, S. N. Smetanin, and A. V. Fedin, "High-average-power SRS conversion of radiation in a $BaWO_4$ crystal," Quantum Electron. **34**(7), 649–651 (2004).
7. X. H. Chen, X. Y. Zhang, Q. P. Wang, P. Li, S. T. Li, Z. H. Cong, Z. J. Liu, S. Z. Fan, and H. J. Zhang, "Diode side-pumped actively Q-switched Nd:YAG/$SrWO_4$ Raman laser with high average output power of over 10 W at 1180 nm," Laser Phys. Lett. **6**(5), 363–366 (2009).
8. O. Kitzler, A. McKay, and R. P. Mildren, "Continuous-wave wavelength conversion for high-power applications using an external cavity diamond Raman laser," Opt. Lett. **37**(14), 2790–2792 (2012).
9. A. McKay, H. Liu, O. Kitzler, and R. P. Mildren, "An efficient 14.5 W diamond Raman laser at high pulse repetition rate with first (1240 nm) and second (1485 nm) Stokes output," Laser Phys. Lett. **10**(10), 105801 (2013).
10. J.-P. M. Feve, K. E. Shortoff, M. J. Bohn, and J. K. Brasseur, "High average power diamond Raman laser," Opt. Express **19**(2), 913–922 (2011).
11. V. Savitski, I. Friel, J. E. Hastie, M. D. Dawson, D. Burns, and A. J. Kemp, "Characterization of single-crystal synthetic diamond for multi-watt continuous-wave Raman lasers," IEEE J. Quantum Electron. **48**(3), 328–337 (2012).
12. R. P. Mildren, M. Convery, H. M. Pask, J. A. Piper, and T. McKay, "Efficient, all-solid-state, Raman laser in the yellow, orange and red," Opt. Express **12**(5), 785–790 (2004).
13. R. P. Mildren, H. Ogilvy, and J. A. Piper, "Solid-state Raman laser generating discretely tunable ultraviolet between 266 and 320 nm," Opt. Lett. **32**(7), 814–816 (2007).
14. I. V. Mochalov, "Laser and nonlinear properties of the potassium gadolinium tungstate laser crystal $KGd(WO_4)_2$:Nd^{3+}-(KGW:Nd)," Opt. Eng. **36**, 1660–1669 (1997).

#204411 - $15.00 USD Received 9 Jan 2014; revised 5 Mar 2014; accepted 6 Mar 2014; published 14 Mar 2014

15. R. P. Mildren, D. W. Coutts, and D. J. Spence, "All-solid-state parametric Raman anti-Stokes laser at 508 nm," Opt. Express **17**(2), 810–818 (2009).
16. R. P. Mildren, "Side-pumped crystalline Raman laser," Opt. Lett. **36**(2), 235–237 (2011).
17. V. V. Filippov, "Athermal directions in $KGd(WO_4)_2$ and $KLu(WO_4)_2$ crystals under uniform heating," Appl. Opt. **52**(18), 4377–4384 (2013).
18. J. E. Hellström, S. Bjurshagen, and V. Pasiskevicius, "Laser performance and thermal lensing in high-power diode-pumped Yb:KGW with athermal orientation," Appl. Phys. B **83**(1), 55–59 (2006).
19. A. McKay, O. Kitzler, and R. P. Mildren, "High power tungstate-crystal Raman laser operating in the strong thermal lensing regime," Opt. Express **22**(1), 707–715 (2014).
20. S. Saghafi, C. Sheppard, and J. A. Piper, "Characterising elegant and standard Hermite-Gaussian beam modes," Opt. Commun. **191**(3–6), 173–179 (2001).
21. K. L. Wlodarczyk, I. J. Thomson, H. J. Baker, and D. R. Hall, "Generation of microstripe cylindrical and toroidal mirrors by localized laser evaporation of fused silica," Appl. Opt. **51**(26), 6352–6360 (2012).
22. W. Lubeigt, G. Valentine, J. Girkin, E. Bente, and D. Burns, "Active transverse mode control and optimization of an all-solid-state laser using an intracavity adaptive-optic mirror," Opt. Express **10**(13), 550–555 (2002).
23. O. Silvestre, J. Grau, M. C. Pujol, J. Massons, M. Aguiló, F. Díaz, M. T. Borowiec, A. Szewczyk, M. U. Gutowska, M. Massot, A. Salazar, and V. Petrov, "Thermal properties of monoclinic $KLu(WO_4)_2$ as a promising solid state laser host," Opt. Express **16**(7), 5022–5034 (2008).
24. A. K. Cousins, "Temperature and thermal stress scaling in finite-length end-pumped laser rods," IEEE J. Quantum Electron. **28**(4), 1057–1069 (1992).
25. W. Koechner, "Thermal Lensing in a Nd:YAG Laser Rod," Appl. Opt. **9**(11), 2548–2553 (1970).
26. P. A. Loiko, K. V. Yumashev, N. V. Kuleshov, G. E. Rachkovskaya, and A. A. Pavlyuk, "Thermo-optic dispersion formulas for monoclinic double tungstates $KRe(WO_4)_2$ where *Re*=Gd, Y, Lu, Yb," Opt. Mater. **33**(11), 1688–1694 (2011).
27. M. M. Mazur, D. Y. Velikovskii, F. A. Kuznetsov, L. I. Mazur, A. A. Pavlyuk, V. E. Pozhar, and V. I. Pustovoit, "Elastic and photoelastic properties of $KGd(WO_4)_2$ single crystals," Acoust. Phys. **58**(6), 658–665 (2012).
28. J. D. Foster and L. M. Osterink, "Thermal effects in a Nd:YAG laser," J. Appl. Phys. **41**(9), 3656–3663 (1970).
29. P. A. Loiko, I. A. Denisov, K. V. Yumashev, N. V. Kuleshov, and A. A. Pavlyuk, "Laser performance and thermal lensing in flashlamp pumped N_p-cut and N_g-cut Nd:KGW crystals," Appl. Phys. B **100**(3), 477–483 (2010).
30. G. M. Bonner, H. M. Pask, A. J. Lee, A. J. Kemp, J. Wang, H. Zhang, and T. Omatsu, "Measurement of thermal lensing in a CW $BaWO_4$ intracavity Raman laser," Opt. Express **20**(9), 9810–9818 (2012).
31. P. A. Loiko, K. V. Yumashev, N. V. Kuleshov, G. E. Rachkovskaya, and A. A. Pavlyuk, "Detailed characterization of thermal expansion tensor in monoclinic $KRe(WO_4)_2$ (where *Re*=Gd, Y, Lu, Yb)," Opt. Mater. **34**(1), 23–26 (2011).

1. Introduction

The end-pumping technique for optical excitation is widely used in lasers for its advantages in providing an intense pump field that has a large volume overlap with the output beam. As waste heat is deposited into the medium in a zone that is narrow compared to the crystal dimensions, the peak on-axis temperatures are heightened compared to pumping schemes that more homogenously excite the medium. The temperature increase and spatial gradients lead to deleterious effects that may include birefringence, lensing, perturbations to phonon and electronic state populations, and in extreme cases lead to crystal fracture. All these effects are of major concern in all high power laser devices including inversion lasers, Raman lasers, and nonlinear frequency convertors. To date, most analysis of thermal induced effects has been conducted in end-pumped lasers operating under steady-state conditions (see for example [1] and references therein). However, it is important to investigate the transient behavior in leading to the establishment of steady-state conditions in order to better understand thermal effects and their role on laser behavior when operating in bursts or with reduced duty-cycle.

Raman lasers are an important class of lasers due to their ability to provide gain in a wide range of the optical spectrum. They are almost always end-pumped, and, being reliant on the inelastic Raman scattering process, the heat generated in the medium is an important consideration when scaling to high power. The thermally-induced temperature gradients are exacerbated in Raman lasers by the strong focusing of the interacting fields that are generally used to ensure efficient conversion. In molecular ion Raman crystals, such as the alkali or alkalis-earth nitrates and tungstates, thermal effects are evident even for average output powers around the single or multi-watt level [2,3]. Higher powers (>5 W) have been obtained by compensating for lensing in the resonator design [4,5], or using materials with improved thermal characteristics such as barium tungstate [6,7] and diamond [8–11]. As part of the on-

#204411 - $15.00 USD Received 9 Jan 2014; revised 5 Mar 2014; accepted 6 Mar 2014; published 14 Mar 2014

going drive for higher powered devices, it is important to understand how the crystal heating affects performance and to determine methods for compensation or circumvention.

Here we consider the temporal development of laser behavior in an end-pumped external cavity Raman laser. The aim is to provide a detailed characterization of the transition to steady-state output to elucidate the various thermal contributions, such as end-face bulging, photo-elastic effects and thermo-optic effects, that critically affect the laser output. The temporal dynamics are also of direct interest for laser applications that require high power output in burst or at reduced duty-cycles. External cavity Raman lasers provide a convenient system for observing the thermal effects in the medium separately for fixed pump beam parameters, as well as being of substantial practical interest as adaptable add-on to a wide range of pump sources.

The laser under investigation was an external cavity Raman laser using potassium gadolinium tungstate (KGW) as the Raman medium. KGW is a non-hydroscopic crystal with high laser damage threshold (10^{10} W/cm^2 for 10 ns pulses) that is versatile in its ability to provide multiple Raman shifts according to the pump polarization [12,13] and to act as a laser ion active host [14]. It is also suitable for anti-Stokes laser generation [15] and for operation using transverse pumping [16]. The gain coefficients for its two strongest Raman modes (768 cm^{-1} and 901 cm^{-1}) are approximately 4 cm/GW at 1064 nm. Being in the monoclinic crystal class, it has anisotropic optical, thermal and mechanical properties. These anisotropies make analysis highly complex but may be potentially exploited for producing characteristic laser behavior or as an interesting method for reducing thermal effects (see, for example, athermal studies of [17,18]). Recently, we found that significant astigmatic thermal lensing in a high power KGW Raman laser was responsible for reduced efficiency and highly elongated output beams [19]. Using a 46 W pump laser, 8.3 W of second-Stokes output power was obtained in an output beam primarily consisting of a 7th-order Hermite-Gaussian (H-G) mode in the X_1' principal direction of the thermal expansion tensor. We now investigate a similar system as a function of duty-cycle and track the transient behavior during each on-time period. We investigate the use of cavity element curvature (spherical and cylindrical) for ameliorating some of the deleterious thermal effects. The results are compared with calculations for the time-dependent temperature field in the crystal that we use to elucidate the possible mechanisms responsible for the observed behavior.

2. Experiment

The system under investigation, which was similar to that previously described in [19], consisted of a Q-switched pump laser of output power 50 W focused into an external cavity KGW Raman laser. The pump laser was Q-switched at 38.6 kHz and produced pulses of duration approximately 25 ns at full width half maximum. The pump beam quality was M^2 ~3.0 in the horizontal direction and M^2 ~3.8 in the vertical direction. The Raman laser, as illustrated in Fig. 1(a), consisted of a two-mirror resonator with the KGW oriented with the crystallographic *a* axis in the vertical direction. Mirrors were selected to maximize second-Stokes output and provide a double pass of the pump beam through the crystal. An isolator was used to prevent back reflections from perturbing the pump laser. The input mirror was planar and transmitted 83% of the pump and reflected more than 99% of the first 1177-nm and second 1316-nm Stokes fields. Three output mirrors were used throughout this work; these had radius of curvature (RoC) of 20 cm, 50 cm and 100 cm and were each less than 15% transmitting at the first Stokes and approximately 68% at the second Stokes radiation. When using the 20-cm curvature end mirror, the resonator had calculated fundamental mode sizes of 387 μm and 409 μm for the first and second Stokes. For these output couplers, the output contained more than 90% at the second Stokes radiation at 1316 nm when operating well above threshold. Minor Stokes lines at 1177 nm and 1205 nm were also observed.

The pump beam was focused into the 45-mm-long KGW crystal to a waist of 105 μm generating at peak intensities of 180 MW/cm^2 at maximum pump power. The pump polarization was linear and aligned along the N_m axis where KGW has maximum gain on the

#204411 - $15.00 USD Received 9 Jan 2014; revised 5 Mar 2014; accepted 6 Mar 2014; published 14 Mar 2014

901 cm^{-1} Raman shift. The 5 × 5 mm^2 crystal faces were broadband anti-reflection coated for the pump and first Stokes radiations.

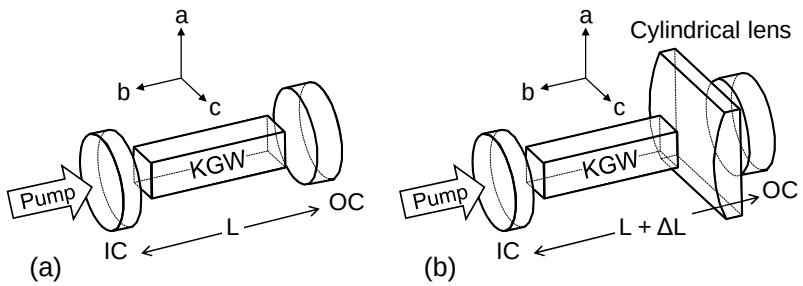

Fig. 1. (a) External cavity KGW Raman laser. (b) External cavity KGW Raman laser with a compensating intracavity cylindrical lens. IC is the input mirror; OC is the output coupler; L = 5 cm and $L + \Delta L$ = 9 cm are the resonator lengths. The *abc* axes refer to the crystallographic axes of KGW.

In order to keep the analysis of Raman laser performance with duty cycle and power as simple as possible, it was important to keep the pump beam temporal and spatial properties constant across the investigated range. We thus kept the pump laser operating at constant current and varied beam parameters using a downstream a rotating half-waveplate and thin-film polarizer. The duty cycle was varied between 15% and 100% using two two-blade rotating chopper wheels at frequencies between 2 and 100 Hz. The output power and near field profiles were obtained in combination with an inline long pass filter to eliminate any residual pump light.

3. Output versus duty cycle

The Raman power as a function of pump power is shown in Fig. 2 for several values of duty cycle (DC) between 15% and 100%. For 100% DC, the threshold was approximately 20 W and the Raman laser generated 7 W at maximum pump power. Output increases linearly with pump power with a discontinuity in the slope that occurs at the 3–4 W level. The transition coincides with a marked change in the spatial properties of the output beam, from circular near TEM_{00} mode to preferential excitation of a H-G mode above the transition at the 3–4 W level [19]. The maximum slope efficiency and absolute conversion efficiencies was 40% and 15%. For 50% DC, the slope efficiency increases to 46% across the full range of operation with a maximum on-time power of 12 W. As DC is reduced further, we observe a progressive reduction in threshold and increase in slope efficiency. For 50%, 33% and 25% DCs, 12.1 W, 13.4 W and 14.8 W was obtained with 26.4%, 29.2% and 32.0% overall efficiencies respectively. For 15% DC, an on-time output power of 17.8 W (2.5 times higher than for 100% DC) was obtained from 46.2 W of incident pump power with a slope efficiency of 52.1% and an overall power conversion of 38.5%. The spatial output beam maintains a Gaussian profile with an $M^2 < 2$ over the entire pumping range. Over the investigated range, reducing DC was found to decrease the laser threshold from approximately 20 W to 16 W.

#204411 - $15.00 USD Received 9 Jan 2014; revised 5 Mar 2014; accepted 6 Mar 2014; published 14 Mar 2014

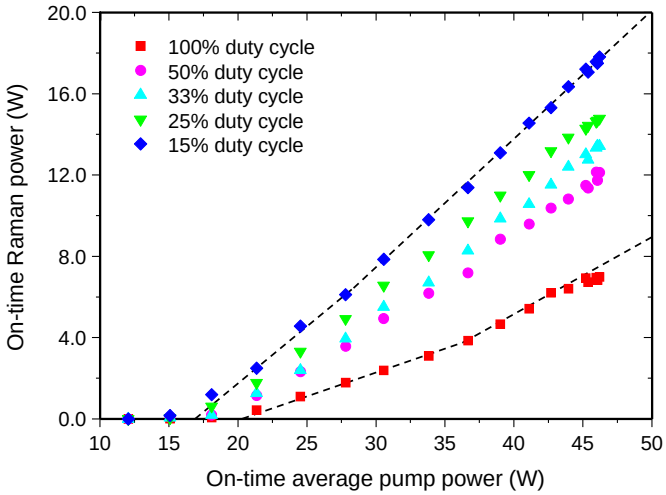

Fig. 2. On-time output power as a function of duty cycle. Dashed lines for the 15% and 100% are shown to highlight the change in threshold as deduced from linear fits to the data.

Figure 3 shows the time behavior of output at maximum power for each DC. The time-integrated intensities for each DC agree well with the maximum output powers of Fig. 2. For longer burst periods, a notable decay in power is evident within a few millisecond of turn-on. The evolution of output was also observed over a 250 ms period using a chopping frequency of 2 Hz as shown in Fig. 4. The peak intensity was averaged over many repeated chopped periods to improve the signal-to-noise ratio. An exponential decay is observed with a time constant of 32 ms.

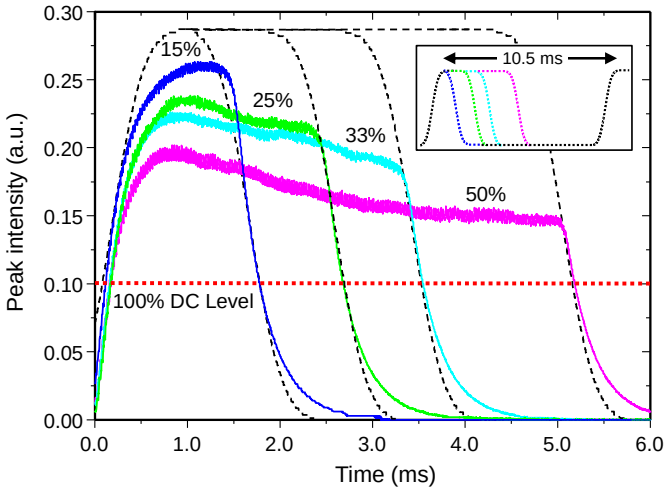

Fig. 3. Relative peak intensities of the Stokes output for duty cycles 15, 25, 33 and 50%. Time traces were electronically filtered using a 4 kHz low pass filter, and each displayed waveform was averaged 500 times. The dashed lines show the calculated transmitted pump intensity by the chopper for pump beam to highlight the approximate rise and fall rate of the pump experienced by the Raman laser. The pump beam was mechanically chopped at 95 Hz.

The near-field beam profile was tracked over the same time frame. A ccd camera was gated on for short 2 ms periods and stepped through the duration of the chopped signal in increments of 2 ms using a digital delay generator. In this way, individual frames showing the development of the near-field profile were built up over successive periods as shown in inset

#204411 - $15.00 USD Received 9 Jan 2014; revised 5 Mar 2014; accepted 6 Mar 2014; published 14 Mar 2014

Fig. 4 and animated in Media 1. Note that the background image seen in the upper and lower sections of images (most notable at t = 0 ms and 32 ms) is an artefact caused by ccd blooming from incident light prior to the gated period.

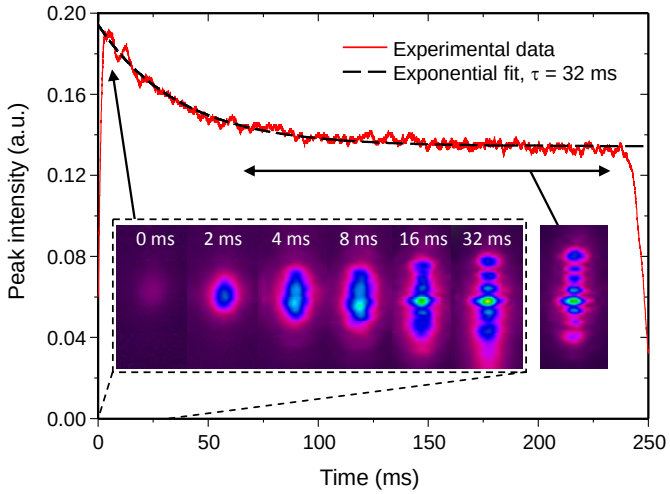

Fig. 4. Relative Stokes intensity (red) with 50% duty cycle pumping at 2 Hz shows an exponential decay (black) with a time constant of 32 ms. The experimental data was electronically filtered using a 10-kHz low pass filter, and was averaged over 256 time traces. Inset images show 2 ms-gated near-field profiles at various times during the pump on-time illustrating the development of high order H-G modes (see also animation in Media 1).

The images show that the near-field profile evolves from a low-order mode to an elongated high-order H-G beam within 20 ms. The rapid evolution of laser modes in the first 20 ms may be responsible for the high frequency structure (~100 Hz) observed in the intensity in this period. By 32 ms, the mode order was $m \approx 7$ which remains relatively constant at later times to 230 ms. The mode order at these later times is the same as for steady-state (100% DC) profile.

4. Output coupling curvature

We have previously proposed [19] that the preferential excitation of high order modes is the result of a strong index gradient producing a defocusing (negative) cylindrical lens with its principal axis closely aligned to the X_1' principal direction of the thermal expansion tensor. In order to confirm this and gain an approximate measure of the lens strength, we investigated output power and beam profiles as a function of mirror curvatures. In Fig. 5, the H-G mode order (in terms of beam propagation factor using the relation $M_y^2 \sim 2m + 1$ where m is the number of nodes in the beam profile [19,20]) is plotted as a function of Raman power for three different end-mirror curvatures. The highest Raman laser power and best beam quality (see Point C in Fig. 5) is obtained for the output coupler with the greatest curvature (20 cm) as expected for a negative lens in the Raman crystal. When reducing mirror curvature, the power and beam quality deteriorate markedly. For a RoC of 100 cm, the maximum power was reduced by more than half and the elongation of the near-field beam profile increased further to m = 15 (corresponding to $M_y^2 \sim 31$).

#204411 - $15.00 USD Received 9 Jan 2014; revised 5 Mar 2014; accepted 6 Mar 2014; published 14 Mar 2014

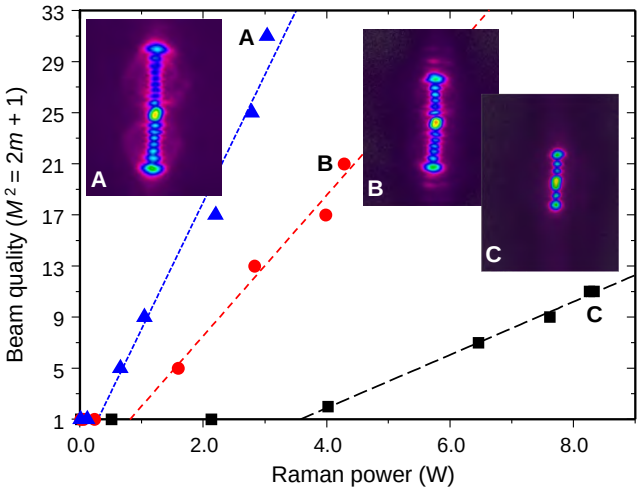

Fig. 5. Beam quality factor in the X_1 direction of the output mode as a function of average Raman output power for the KGW Raman laser operating with three different end-mirror curvatures (triangles 100 cm; circles 50 cm; and squares 20 cm). Insets show the near-field profiles of the Raman output beam at the highest pump power (45 W) with output power and beam quality shown by points A, B and C.

The mode order increases linearly with Stokes power beyond a Stokes threshold power that is inversely related to the radius of curvature of the end-mirror. The threshold indicates the point at which the induced lens begins to substantially perturb the TEM_{00} mode in the crystal. Using ABCD matrix analysis, we calculated the thermal lens strength for which the resonator becomes unstable for the TEM_{00} mode. The analysis used a cylindrical lens placed at the resonator midpoint to simulate the KGW thermal lens. Although the validity of ABCD analysis is questionable for the present situation in which the gain and index profile in the KGW is not quadratic across the entire beam profile, this approach is expected to enable us to determine an approximate rate for scaling of the KGW lens strength with Raman power. This procedure finds that the focal lengths for the 100 cm, 50 cm and 20 cm end-mirror resonators are −530 mm, −293 mm and −128 mm respectively at threshold points of 0.29 W, 0.81 W and 3.57 W of Raman output power. The relationship between thermal lens strength and Raman power is thus approximately linear at a rate of $-1.7\ m^{-1}$ per watt of Raman power. It should be noted that heating contributions to the crystal from impurity absorption at the Stokes and pump wavelengths are likely to be significant and thus the explicit lens strength dependence on Raman power assumed here is approximate.

We noted that the near-field beam images at very high order sometimes exhibited a clear angular displacement between the upper and lower halves of the beam profile as can be seen most clearly in inset A and B of Fig. 5. This interesting feature was observed for very high mode orders and for some cavity alignments. Although more work is required to understand its origin, we tentatively suggest it may result from a combination of cavity alignment in the horizontal direction in the presence of a complex anisotropic lens in the Raman crystal.

5. Compensation using an intracavity cylindrical lens

In order to provide compensation for the negative cylindrical thermal lens we placed a positive cylindrical lens inside the resonator as illustrated in Fig. 1(b). The focal length of 5 cm was chosen to provide an approximately equal and opposite lens at the maximum power level based on the lens susceptibility value determined above. The resonator length was increased to 9 cm to accommodate the cylindrical lens and mount. Performance was compared with and without compensating lens for the fixed cavity length. At maximum pump power the compensated Raman laser oscillated with more than 7.6 W with an approximate

#204411 - $15.00 USD Received 9 Jan 2014; revised 5 Mar 2014; accepted 6 Mar 2014; published 14 Mar 2014

threshold of 26.8 W. The slope efficiency was approximately 30%. In comparison, as shown in Fig. 6, without the compensating lens the Raman laser has a maximum output power of 2.6 W with a threshold close to 36 W and notably lower slope efficiency. The reduced output power compared to the 7 W seen for the short cavity is expected as a result of reduced pump-Stokes overlap and the longer time required to build-up a Stokes pulse within the pulse gain period.

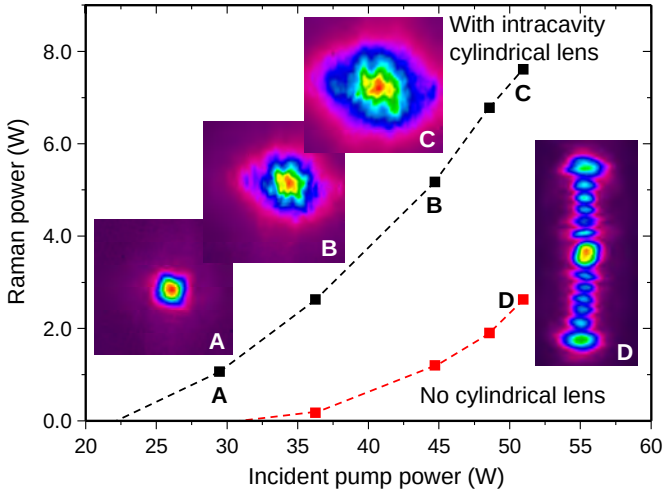

Fig. 6. Output power of the combined Stokes radiation from the KGW Raman laser with (black) and without (red) compensating cylindrical lens. Inset show typical near-field profiles of the Raman output beam at selected power levels.

The near field profiles for both cases are also shown in Fig. 6. The compensated beam profile remains rotational symmetric and single lobed, indicating a much more balanced net lens strength in the two directions. Notable high frequency structure is observed at high power levels indicating some substantial residual aberrations in the Raman medium that are not purely cylindrical. Improved compensation could be achieved, for example, intracavity phase plates or adaptive mirrors such as those used in [21,22]. The beam profile without the compensating lens is a H-G mode of order notably higher than that seen with the shorter cavity.

6. Analysis and discussion

6.1 Evolution of axial temperature and temperature gradient calculations

We use numerical calculations of the internal crystal temperature as direct measurements are presently challenging. The spatio-temporal development of temperature was calculated using finite element analysis using a transient heat solver (QuickField; Tera Analysis Ltd). The package uses finite element analysis to solve Laplace's equation for heat diffusion in two spatial dimensions. A variable mesh and time spacing were used to enable adequate step-sizes for the geometry and temporal evolution. Power deposition was assumed to be continuous with a Gaussian profile of radius equal to the pump waist radius (105 μm) on the crystal axis and evenly distributed along the crystal length. The external crystal face was assumed to be fixed at constant temperature (Dirichlet boundary condition). Model input included specific heat (0.3 J g^{-1} K^{-1}), density (ρ = 7.3 g cm^{-3}), and thermal conductivity, which for KGW is anisotropic with values shown in Table 1 for *a* and *c* crystal directions. (We note that the principal directions of the thermal conductivity tensor are more likely to be aligned to the thermal expansion tensor based on results published for KLuW [23].) For the investigated power deposition values (typically 10–20% of the Stokes power and up to a few watts), the maximum temperature increases are sufficiently small (less than 20 K) to assume constant

#204411 - $15.00 USD Received 9 Jan 2014; revised 5 Mar 2014; accepted 6 Mar 2014; published 14 Mar 2014

thermal conductivity. As a result, the spatio-temporal temperature behavior is independent of the absolute temperature and we express the model output normalized to 1 W of deposited power.

Table 1. Optical, Mechanical and Thermal Properties for KGW used in this Study.

Parameter	Direction			Unit	Ref.
	N_m	N_g	N_p		
n_o	1.99	2.03	1.94		[14]
dn/dT	–11.8	–17.3	–15.7	10^{-6} K^{-1}	[26]
	X_1	X_2	X_3		
α_T	7.6	1.7	20.6	10^{-6} K^{-1}	[31]
	a	b	c		
κ	2.6	3.4	3.8	W/(m·K)	[14]

The evolution of on-axis temperature is shown in Fig. 7(a). The temperature profile increases to a steady state value of 3.7 K/W with a time constant of approximately 1 s. Beyond 2 s the on-axis temperature is within 5% of the steady-state value. As many of the thermal processes that affect laser performance are caused by the radial temperature gradient dT/dr (or d^2T/dr^2 see below), it is valuable to also show the rate at which the maximum gradient in the crystal evolves. The maximum gradient occurs near the pump beam radius. As also shown in Fig. 7 for the crystal *a* direction, the gradient evolves rapidly in the first 50 ms and slowly thereafter. Since we observe laser power and beam properties on this time scale (τ = 32 ms—refer Fig. 4) and much faster than the evolution of temperature, it is deduced that gradients are the main cause of reduced efficiency and multimode spatial properties.

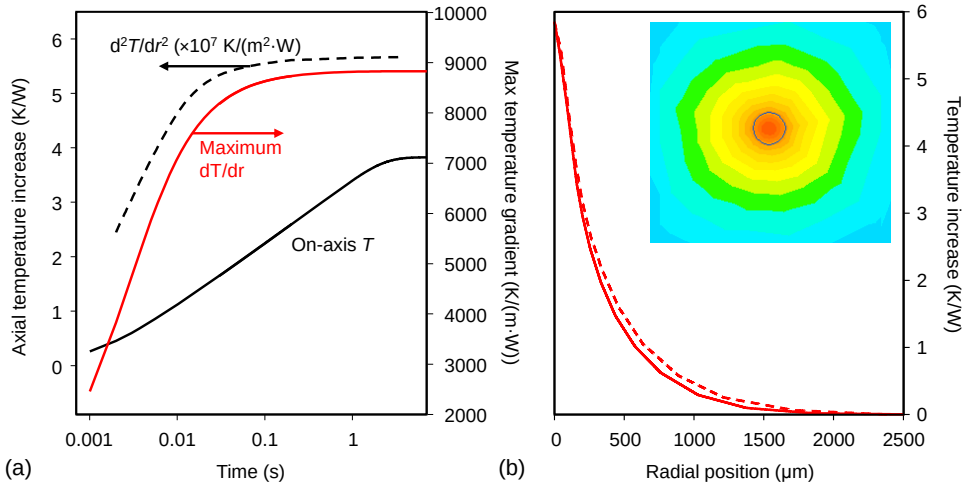

Fig. 7. (a) Calculated on-axis temperature (black solid) and maximum temperature gradient in the crystal *a*-direction (red) as a function of time from turn-on at t = 0 s. Temperatures are expressed in per watt of power deposited in the crystal. The quadratic coefficient (d^2T/dr^2) was determined by curve fits to data within the beam radius. (b) The temperature as a function of radius in the vertical (*a*-direction - solid) and horizontal (dotted) directions for t = 200 ms. The 2-D map inset provides a visual indication of the axial symmetry of the temperature profile (the pump waist circle of radius 105 μm is shown for scale).

#204411 - $15.00 USD Received 9 Jan 2014; revised 5 Mar 2014; accepted 6 Mar 2014; published 14 Mar 2014

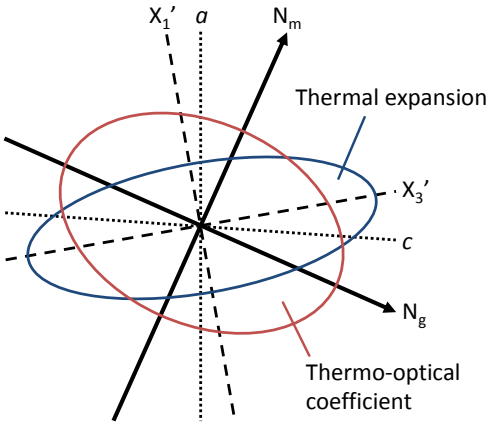

Fig. 8. Relative strengths of the thermal expansion and thermo-optic coefficients of KGW in plane transverse to the N_p beam axis. The crystallography *a* and *c* (dotted), thermal expansion X_1' and X_3' (dashed), and thermo-optical N_m and N_g (solid lines) axes are overlaid.

6.2 Effects of thermal gradients

Thermal gradients lead to index gradients through the thermo-optic effect and induce stresses that cause wavefront distortion via end-face distortion (end-face bulging) and material photo-elasticity. Such effects have been studied in depth for end-pumped lasers involving media such as Nd:YAG and a small number of anisotropic crystals. Usually end-pumped crystals are sufficiently short that the stresses out of the transverse plane can be assumed to be small (i.e., the plane stress approximation) [1,24]. In the present case of a thin heated region in a relatively long crystal, this approximation is unlikely to be valid and a more general treatment is required. Such a treatment would require a detailed knowledge of tensorial thermal, mechanical and optical coefficients of KGW, which to date have not been published in detail. Instead, here we discuss qualitatively the lensing contributions separately in the KGW crystal with the aim of deducing the major mechanisms dictating laser behaviour.

6.2.1 Thermo-optical

The lens contribution introduced from the thermal optical effect can be estimated from the calculated temperature and using published values for d*n*/d*T* as show in Table 1. For a parabolic temperature gradient, the induced lens strength is calculated using

$$f_{(1)}^{-1} = n_0 \cdot l \cdot \frac{\mathrm{d}n}{\mathrm{d}T} \cdot \left(\frac{\mathrm{d}^2 T}{\mathrm{d}r^2} \right), \qquad (1)$$

where $n_0 = n_0$ (N_m) is the refractive index experienced by the Stokes beam and l is the crystal length. At steady-state, the calculated $\mathrm{d}^2T/\mathrm{d}r^2$ value in the beam region is 6×10^7 K.m^{-2} per watt of power deposited which gives a lens strength susceptibility of the order of –50 m^{-1} per Watt of deposited power. The large strength of this lens component is an indication of the tight focusing in the crystal which leads to large on-axis temperature increase and large radial gradients. The anisotropy in transverse κ values (κ_c/κ_a = 75%) causes an inversely proportional asymmetry in the temperature gradient (see Fig. 7b). Thus thermo-optic effects are expected to lead to a commensurate enhancement in the lens strength along one principal direction of the thermal conductivity tensor (the direction most closely aligned to the *a*-axis). However, since the observed beam elongation is so much greater along one of the axes, we deduce that thermo-optic effects are not the primary cause for the beam asymmetry.

#204411 - $15.00 USD Received 9 Jan 2014; revised 5 Mar 2014; accepted 6 Mar 2014; published 14 Mar 2014

6.1.2 End-face distortion

Distortion of the shape of the crystal end-faces due to differential thermal expansion also contributes to lensing of the beam. For the purposes of comparing the likely magnitude and sign of the induced lens, we gain an estimate by assuming an isotropic material by following the approach in Koechner [25]. In this case the lens strength contribution is

$$f_{(2)}^{-1} = -2\left(n_0 - 1\right)\alpha_T r_0 \left(\frac{\mathrm{d}^2 T}{\mathrm{d}r^2}\right). \tag{2}$$

We take $\alpha_T = \alpha_T\,(X_2')$ as the thermal expansion coefficient along the optical axis, and r_0 as the rod radius, the approximate distance over which the buckling of the crystal shape takes place. Using the above value for the $\mathrm{d}^2T/\mathrm{d}r^2$, the lens strength susceptibility due to end-face bulging is + 36 m^{-1} per watt, a value of similar magnitude to the thermo-optic contribution but of opposite sign.

A calculation that takes into consideration the material anisotropy can be achieved (in principle) by solving generalized Hooke's Law (see for example [1]) using published values for the thermal expansion [26] and elastic tensors [27] for the anisotropic material. It would be interesting to undertake such a study to determine the level of asymmetry in the distorted facet. Since the distortion only introduces a positive lens, its only mechanism for introducing the observed beam symmetry would be through counteracting a large negative component introduced by another mechanism (e.g., the thermo-optic lens). We suggest that this is mechanism is also unlikely to be responsible for the observed beam asymmetry as it would imply an unusually large anisotropy in KGW's elasticity tensor.

6.1.3 Photo-elastic

Differential expansion causes stress which in turn alters the refractive index according the photo-elastic effect. The refractive index and stress-induced mechanical strain are related via the change in optical indicatrix (see for example [25])

$$\Delta B_i = P_{ij}\varepsilon_j \tag{3}$$

where the photo-elastic tensor P_{ij} and strain tensor ε_j are in reduced form and a sum over j is implied. Note that we consider only the mechanical stress contribution to the photo-elastic induced lensing as in refs [24,28], and assume a zero photo-elastic contribution from thermal strain. This is justified by the fact that material photoelastic coefficients (such as those for KGW [27]) are determined from experiments involving only mechanical stress. The effect of thermal strain on refractive index is taken into account explicitly in the thermo-optic effect. Although other others have combined thermal and mechanical strain together [1,24] in the evaluation of photo-elastic effects, such approaches may lead to significant errors and require a more complex treatment involving a redefinition of the thermo-optic coefficient [1]. The change in refractive index $\Delta n_i = -0.5 {n_0}^3 \Delta B_i$ is then

$$\Delta n_i = -0.5 n_0^3 P_{ij}\varepsilon_j. \tag{4}$$

Evaluation of the induced lens requires calculation of all the normal and shear strain components and a good knowledge of P_{ij}. In isotropic materials, crystal heating on-axis is well known to cause radially-directed compressive strain (negative ε) in the beam region as a result of the stress induced as the inner hot zone expands into the outer cooler material [24]. For KGW, thermal expansion is strongly anisotropic in the transverse plane. As shown in Fig. 8, $\alpha_T\,(X_3)$ is three times larger than $\alpha_T\,(X_1)$ and as a result the compressive strain will be larger in this direction. In order to gain an estimate for the relative lensing contributions due to the radial compression, we assert that the compressive strain is approximately proportional to the thermal expansion in each direction $\varepsilon_j \sim \alpha_{Tj}.\Delta T_j$. Thus the compression in the X_3-direction is likely to be much stronger than for X_1. It is also necessary to consider axial strain components

#204411 - $15.00 USD Received 9 Jan 2014; revised 5 Mar 2014; accepted 6 Mar 2014; published 14 Mar 2014

since the plane stress approximation breaks down for the present geometry. We expect these to be significant for the long thin heated region, especially for the shear components ($\varepsilon_{4,6}$) as the heated central region expands axially inside the cooler outer region.

Although the P_{ij} coefficients have not been published for KGW to the authors' knowledge, we use values for the acousto-optic quality M_2 and acoustic velocity v [23,27], to gain indicative absolute values using

$$\left|P_{ij}\right| = \sqrt{\frac{M_2 r v^3}{n_0^6}}. \tag{5}$$

Table 2 shows the relevant values for light polarized close to the crystal *a*-direction which provides a good approximation to the present case for N_m polarized light. The two P_{ij} corresponding values to compression in the *a* (~X_1) and *c* (~X_3) directions are approximately equal. Thus the relative lens strength in each direction is dominated by the thermal expansion anisotropy in the ratio of approximately α_T (X_1): α_T (X_3) = 1:2.7. Thus for radial compression to be responsible for beam elongation in the X_1 direction its action must be, as noted for end-face distortion, to counteract a large negative lens in the X_3 direction induced by another mechanism.

Table 2. Photo-elastic Coefficients Derived from Acousto-optic Measurements of [27].

Compressional sound wave			Photo-elastic tensor	
Direction	v (km/s)	M_2 (10^{-16} s^3/kg)	P_{ij}	Absolute Value
A	5.06	7.5	P_{11}	0.103
C	2.59	61	P_{13}	0.108

Shear stresses in the X_1-X_2 and X_3-X_2 directions are potentially much more important causes for the beam asymmetry. The M_2 values for shear acoustic waves can be up to two orders of magnitude larger than for the longitudinal waves [27], which, depending upon their velocity, can lead to major enhancements in the relevant P_{ij}. Thus the observed negative lens in the X_1 direction may be a result of an enhanced value of P_{16}, which relates shear stress in the X_1-X_2 direction to n_0 (N_m). The value for P_{14}, the relevant coefficient for the shear stress in the X_3-X_2 direction, would then either be much smaller or of opposite sign. Since shear stresses are much more important for longer crystals, this may explain the contrasting thermal lensing characteristics observed in much shorter Nd:KGW rod lasers [17,18,29]. High shear stresses may also be responsible for the astigmatic lensing with a strong negative lens component also observed in tetragonal tungstate Raman crystals such as $BaWO_4$ [30].

7. Conclusions

In summary we have investigated the dynamical thermal lens and modal properties in a high-average power external cavity KGW Raman laser. From 46 W of on-time pump power, Raman on-time 18 W was demonstrated at 15% duty-cycle, more than a two-fold higher than the maximum steady-state power. The evolution of the thermal lens and mode structure develops to the steady-state conditions within tens of milliseconds consistent with the establishment of thermal gradients in the crystal.

A preliminary analysis of the thermal lens contributions suggests photo-elastic effects are the major cause of the lens asymmetry for the present case of end-pumped long crystals, most probably as a result of the differential expansion in the transverse plane and shear stresses in the X_1-X_2 and X_3-X_2 directions. Improved knowledge of the photo-elastic coefficients, particularly those corresponding to shear stresses in the axial direction, is required to allow more quantitative treatment.

Acknowledgments

This material is based on research sponsored by the Australian Research Council Future Fellowship (FT0990622) and Discovery Grant (DP130103799) Schemes, and the US Air Force Research Laboratory under agreement number FA2386-12-1-4055.

Optics Express

Title Details

Related Titles

- **Alternative Media Edition** (1)
- **Supplement** (1)

Lists

Marked Titles (0)

Search History

1094-4087
0048-9697
1068-7971
0898-929X
1039-7116
1471-2164
0094-8276
1279-7707

Basic Description

Title	Optics Express
ISSN	1094-4087
Publisher	Optical Society of America
Country	United States
Status	Active
Start Year	1997
Frequency	Bi-weekly
Language of Text	Text in: English
Refereed	Yes
Abstracted / Indexed	Yes
Open Access	Yes http://www.opticsexpress.org
Serial Type	Journal
Content Type	Academic / Scholarly
Format	Online
Website	http://www.opticsinfobase.org/oe/journal/oe/about.cfm
Email	opex@osa.org
Description	Covers original research in optical science and technology.

- **Subject Classifications**
- **Additional Title Details**
- **Publisher & Ordering Details**
- **Online Availability**
- **Abstracting & Indexing**
- **Other Availability**
- **Demographics**
- **Reviews**

Save to List Email Download Print Corrections Expand All Collapse All